



1 An Improved Hydrometeor Detection Method for Millimeter-Wavelength Cloud

2 Radar

3 Ge Jinming¹, Zhu Zeen¹, Zheng Chuang¹, Xie Hailing¹, Zhou Tian¹, Huang Jianping¹,

4 and Fu Qiang^{1,2}

5 ¹Key Laboratory for Semi-Arid Climate Change of the Ministry of Education and

6 College of Atmospheric Sciences, Lanzhou University, Lanzhou, 730000, PRC

7 ²Department of Atmospheric Sciences, University of Washington, Seattle, WA,

8 98105, USA

9

10

11

12

13

14

15

16

17

18

19

20

21

22



23 Abstract

24 A new method is proposed to distinguish clouds and other hydrometeors from noise
25 in cloud radar observations. Instead of examining radar return for significant levels of
26 signals, which is used in current cloud radar hydrometeor detection algorithms, this new
27 method extracts signals by first reducing noise distribution to a narrow range. “Square
28 clouds” were constructed to test the two schemes. We applied our method to two
29 months of cloud radar observations, and compared the results with those obtained by
30 applying the U.S. Department of Energy (DOE) Atmospheric Radiation Measurements
31 (ARM) program operational algorithm. It was found that our method has significant
32 advantages in recognizing clouds with weak signal and reducing the rates of both failed
33 negative and false positive hydrometeor identifications.



34 1. Introduction

35 Clouds, which are composed of liquid water droplets, ice crystals or both, move
36 around our planet and cover about two-thirds of the earth surface at any time [e.g., *King*
37 *et al.*, 2013]. By reflecting solar radiation back to the space (the albedo effect) and
38 trapping thermal radiation emitted by the Earth surface and the lower troposphere (the
39 greenhouse effect), clouds strongly modulate the radiative energy budget in the climate
40 system [e.g., *Fu*, 2007; *Fu et al.*, 2002; *Huang et al.*, 2006a; *Huang et al.*, 2006b;
41 *Ramanathan et al.*, 1989; *Su et al.*, 2008]. Clouds are also a vital stage of water cycle
42 by connecting the water-vapor condensation and precipitation. Despite the importance
43 of clouds in the climate system, they cannot be accurately represented in climate models
44 [*Williams and Webb*, 2009], which causes the largest uncertainty in the predictions of
45 climate change by general circulation models (GCMs) [e.g., *Randall*, 2007; *Stephens*,
46 2005; *Williams and Webb*, 2009].

47 Cloud formation, evolution and distribution are governed by complex physical and
48 dynamical processes on a wide range of scales from synoptic motions to turbulence
49 [*Bony et al.*, 2015]. Unfortunately, the processes that occur on smaller spatial scales
50 than a GCM grid box cannot be resolved by current climate models and the coupling
51 between large scale fluctuations and cloud microphysical processes are not well
52 understood [e.g., *Huang*, 2006; *Mace et al.*, 1998; *Yan et al.*, 2015; *Yuan et al.*, 2006].
53 Moreover, the cloud horizontal inhomogeneity and vertical overlap are not resolved by
54 GCMs [*Barker*, 2000; *Barker and Fu*, 2000; *Fu et al.*, 2000a; *Fu et al.*, 2000b; *Huang*
55 *et al.*, 2005; *Li et al.*, 2015]. To better understand cloud processes for improving their



56 parameterization in climate models and revealing their evolution in response to climate
57 change, long-term continuous observations of cloud fields in terms of both macro- and
58 micro-physical properties are essential [e.g., *Ackerman and Stokes*, 2003; *Sassen and*
59 *Benson*, 2001; *Thorsen et al.*, 2011; *Wang and Sassen*, 2001].

60 Millimeter-wavelength Cloud Radars (MMCRs) are powerful instruments that can
61 resolve cloud vertical structure for their occurrences and microphysical properties [e.g.,
62 *Clothiaux et al.*, 1995; *Kollias et al.*, 2007a; *Mace et al.*, 2001]. The wavelengths of
63 MMCRs are shorter than those of weather radars and they have excellent sensitivity to
64 cloud droplets and ice crystals and can penetrate multiple cloud layers [e.g., *Kollias et*
65 *al.*, 2007a]. Because of their outstanding advantages for cloud research, millimeter-
66 wavelength radars have been deployed on various research platforms including the first
67 space-borne millimeter-wavelength Cloud Profiling Radar (CPR) onboard the CloudSat
68 [*Stephens et al.*, 2002]. Ground-based MMCRs are operated in the U.S. Department of
69 Energy's Atmospheric Radiation Program (ARM) observational sites [e.g., *Ackerman*
70 *and Stokes*, 2003; *Clothiaux et al.*, 2000; *Clothiaux et al.*, 1999; *Kollias et al.*, 2007b;
71 *Protat et al.*, 2011] and in Europe [*Illingworth et al.*, 2007; *Protat et al.*, 2009]. In July
72 2013, a new generation of Ka band Zenith Radar (KAZR) was deployed in China at the
73 Semi-Arid Climate and Environment Observatory of Lanzhou University (SACOL) site
74 (latitude: 35.946°N; longitude: 104.137°E; altitude: 1.97 km) [*Huang et al.*, 2008],
75 providing an opportunity to observe and reveal the detailed structure of the mid-latitude
76 clouds over East Asia semi-arid regions.

77 Before characterizing the cloud physical properties from the cloud radar return signal,



78 we first need to distinguish and extract the hydrometeor signals from the background
79 noise (i.e. cloud mask). A classical cloud mask method was developed in Clothiaux et
80 al.[2000; 1995] by analyzing the strength and significance of returned signals. This
81 method consists of two main steps. First any power in a range gate that is greater than
82 a mean value of noise plus one standard deviation is selected as a bin containing
83 potential hydrometer signal. Second, a spatial-time coherent filter is created to estimate
84 the significance level of the potential hydrometer bin signal to be real. This cloud mask
85 algorithm is operationally used for the ARM MMCRs data analysis and was later
86 successfully modified and adopted to the CPR onboard the CloudSat [*Marchand et al.*,
87 2008].

88 It is recognized that by visually examining a cloud radar return image, one can easily
89 tell where the return power is likely to be caused by hydrometeors and where the power
90 is just from noise. This ability of human eye on extracting and analyzing information
91 from an image has been broadly studied in image processing and computer vision, and
92 a number of mathematical methods for acquiring and processing information from
93 images have been developed, including some novel algorithms for noise reduction and
94 edge detection [*Canny*, 1986; *He et al.*, 2013; *Marr and Hildreth*, 1980; *Perona and*
95 *Malik*, 1990]. In this paper we develop a new cloud mask method for cloud radar by
96 noticing that removing noise from signal and identifying cloud boundaries are the
97 essential goals of cloud mask. This method reduces the radar noise while preserving
98 cloud edges by employing the bilateral filtering that is widely used in the image
99 processing [*Tomasi and Manduchi*, 1998]. The power weighting probability method



100 proposed by Marchand et al.[2008] is also adopted in our method to prevent the cloud
101 corners from being removed. It is found that our improved hydrometeor detection
102 algorithm is more efficient in terms of reducing false positives and negatives as well as
103 identifying cloud features with weak signals such as thin cirrus clouds.

104 The KAZR deployed at the SACOL is described in section 2 and the new cloud mask
105 algorithm is introduced in section 3. The applications of the new scheme to both
106 hypothetical and observed cloud fields including a comparison with previous schemes
107 are shown in section 4. Summary and conclusions are given in section 5.

108

109 2. The KAZR Radar

110 The SACOL KAZR, built by ProSensing Inc. of Amherst, MA, is a zenith-pointing
111 cloud radar operating at approximately 35 GHz for the dual-polarization measurements
112 of Doppler spectra. The main purpose of the KAZR is to provide vertical profiles of
113 clouds by measuring the first three Doppler moments: reflectivity, radial Doppler
114 velocity, and spectra width. The linear depolarization ratio [Marr and Hildreth, 1980]
115 can be computed from the ratio of cross-polarized reflectivity to co-polarized
116 reflectivity.

117 The SACOL KAZR has a transmitter with a peak power of 2.2 kw and two modes
118 working at separate frequencies. One is called “chirp” mode that uses a linear-FM
119 (frequency modulation) pulse compression to achieve high radar sensitivity of about -
120 65 dBZ at 5 km altitude. The minimum altitude (or range) that can be detected in chirp
121 mode is approximately 1 km AGL. To view clouds below 1 km, a short pulse or “burst



122 mode” pulse is transmitted at a separate frequency just after transmission of the chirp
123 pulse. This burst mode pulse allows clouds as low as 200 m to be measured. The chirp
124 pulse is transmitted at 34.890 GHz while the burst pulse is transmitted at 34.830 GHz.
125 These two waveforms are separated in the receiver and processed separately.

126 The pulse length is approximately 300 ns (giving a range resolution of 45 m), while
127 the digital receiver samples the return signal every 30 m. The interpulse period is 208.8
128 μ s, the number of coherent averages is 1, and the number of the fast Fourier transform
129 (FFT) points is currently set to 512. An unambiguous range is thus 31.29 km, an
130 unambiguous velocity is 10.29 m/s, and a velocity resolution of is 0.04m/s. The signal
131 dwell time is 4.27s. These operational parameters are set for the purpose of having
132 enough radar sensitivity and accurately acquiring reflectivities of hydrometeors. In this
133 study, we mainly use radar observed reflectivity (dBZ) data to test our new hydrometeor
134 detection method.

135 3. Hydrometeor detection algorithm

136 The basic assumption in the former cloud mask algorithms [*Clothiaux et al.*, 1995;
137 *Marchand et al.*, 2008] is that the random noise power follows the normal distribution.
138 In this study, several clear sky cases in all seasons from the KAZR observations were
139 firstly selected to analyze its background noise power distributions (Fig.1). However,
140 as demonstrated in Fig.1a for a clear-sky case during 0000 to 1200 UTC on January
141 21st, 2014, the noise power, which includes both internal and external sources, has an
142 apparent non-Gaussian distribution with a positive skewness of 1.40. The signal-to-
143 noise ratio (SNR) is defined as:



$$144 \quad \text{SNR} = 10 \log \left(\frac{P_s}{P_n} \right) \quad (1)$$

145 where P_s is the power received at each range gate in a profile, P_n is the mean noise
146 power that is estimated by averaging the return power in the top 30 range gates which
147 are between 16.8 and 17.7 km AGL. Since this layer is well above the tropopause, few
148 atmospheric hydrometeors existing in this layer can scatter enough power back to
149 achieve the radar sensitivity. Figure 1 shows that the SNRs for clear skies closely follow
150 a Gaussian distribution. Note that the mean value of the SNR for the noise power is not
151 zero, but a small negative value of about -0.3. This is because the SNR for the noise
152 does not exactly obey the Gaussian distribution. It is further noted that the distribution
153 of SNR and its mean for the top 30 range gates are the same as those from the lower
154 atmosphere. Instead of using radar received power, the SNR is used to estimate the
155 background noise level and taken as the input to the cloud mask procedure.

156 The SNR value is treated as the brightness of a pixel in an image $f(x,y)$ in our
157 hydrometeor detection method. In an image processing, the randomly Gaussian-
158 distributed noise can be smoothed out by using a low pass filter, which gives a new
159 value for a pixel of an image by averaging with neighboring pixels [Tomasi and
160 Manduchi, 1998]. The cloud signals are highly correlated in both space and time and
161 have more similar values in near pixels while the random noise values are not correlated.
162 Therefore, as illustrated in Fig. 2a, this low pass filter can efficiently reduce the original
163 radar noise represented by the green line to a narrow bandwidth (blue line) while
164 keeping the signal preserved. By reducing the standard deviations of noise, which
165 shrinks the overlap region of signal and noise and enhances their contrast, the weak



166 signals (yellow area) that cannot be detected based on original noise level may become
167 distinguished.

168 Based on this idea, we develop a non-iterative hydrometeor detection algorithm by
169 applying a noise reduction and a central pixel weighting schemes. Figure 3 shows the
170 schematic flow diagram of our method. The input SNR data set is first separated into
171 two groups. One group with values greater than the mean background noise SNR (S_o)
172 plus three times of its standard deviation (σ_o) are considered as the cloud features that
173 can be confidently identified. Another group with values between S_o and $S_o + 3\sigma_o$
174 may potentially contain moderate ($S_o + \sigma_o < SNR \leq S_o + 3\sigma_o$) to weak ($S_o < SNR \leq$
175 $S_o + \sigma_o$) cloud signals, which will further go through a noise reduction process. Here
176 S_o and σ_o are estimated from the top 30 range gates of each five successive profiles.

177 The noise reduction process is mainly performed by convolving radar SNR time-
178 height data with a low pass filter. The Gaussian Filter, which outputs a 'weighted
179 average' of each pixel and its neighborhood with the average weighted more towards
180 the value of the central pixel (v_0), is one of the most common functions of the noise
181 reduction filter. A 2-D Gaussian distribution kernel, shown in Fig. 2b₁, can be expressed
182 as:

$$183 \quad G(i, j) = \frac{1}{2\pi\sigma^2} \exp\left(-\frac{i^2+j^2}{2\sigma^2}\right) \quad (2)$$

184 where i and j are the indexes in a filter window which are 0 for the central pixel, and σ
185 is standard deviation of the Gaussian distribution for the window size of the kernel.
186 Equation (2) is used in our study to filter the radar SNR image. Note that the
187 convolution kernel is truncated at about three standard deviations away from the mean



188 in order to accurately represent the Gaussian distribution. Figure 1b are the cumulative
189 distribution functions (CDFs) of clear sky SNR by convolving the same data in Fig. 1a
190 with four filters that have different kernel sizes (3×3 , 5×5 , 7×7 and 9×9 pixels)
191 corresponding to the σ ranging from 0.5 to 2. The original SNR values are distributed
192 from about -5 to 5. After convolving the image with the Gaussian filter, the SNR
193 distribution can be constrained to a much narrower range. It is clear that the filter with
194 a larger kernel size is more effective in suppressing the noise. Shown in Fig. 1c are
195 results for a cloudy case on January 4th, 2014 by applying the filter to the range gates
196 inside the cloud but adjacent to the boundary, showing that a larger kernel size shifts
197 the SNR farther away from the noise region. It therefore appears that increasing the
198 standard deviation (i.e. the window size) continues reducing the noise and increasing
199 the contrast between signal and noise more effectively. On the other hand, a larger
200 kernel can also attenuate or blur the high frequency components of an image (e.g., the
201 boundary of clouds) more at the same time. As shown in Fig. 1d, when the window size
202 is increased from 3×3 ($\sigma=0.5$) to 9×9 ($\sigma=2$), the SNR distribution of the range gates
203 that are outside the cloud but adjacent to the boundary gradually move toward larger
204 values. This will consequently raise the risk of misidentifying cloud boundaries. To
205 solve this problem, a bilateral filtering idea proposed by *Tomasi and Manduchi* [1998]
206 is adopted here. Considering a sharp edge between cloudy and clear region as shown in
207 Fig. 2b₂, we define a $\delta(i, j)$ function that when the central pixel is on the cloudy or
208 clear side, gives a weighting of 1 to the similar neighboring pixels (i.e. on the same
209 side), and 0 to the other side. After combining this δ function to the Gaussian kernel



210 in Fig. 2b₁, we can get a new non-linear function called bilateral kernel as shown in Fig.
211 2b₃. It can be written as:

$$212 \quad B(i, j) = \frac{1}{2\pi\sigma^2} \exp\left(-\frac{i^2+j^2}{2\sigma^2}\right) \cdot \delta(i, j). \quad (3)$$

213 Thus the bilateral kernel will prevent averaging noises with signals, and vice versa. The
214 noise-reduced image $h(x, y)$ is produced by convolving the bilateral kernel with the
215 input image $f(x, y)$ as:

$$216 \quad h(x, y) = k^{-1}(x, y) \sum_{j=-w}^{j=w} \sum_{i=-w}^{i=w} f(x+i, y+j) \cdot B(i, j) \quad (4)$$

217 where $\pm w$ is the bounds of the finite filter window, $k^{-1}(x, y)$ is defined as
218 $1 / \sum_{j=-w}^{j=w} \sum_{i=-w}^{i=w} B(i, j)$ which is used to normalize the weighting coefficients. Since
219 the bilateral kernel function only average the central pixel with neighbors on the same
220 side (Fig. 2b), ideally it will preserve sharp edges of a target. We will discuss how to
221 construct the δ function in order to group the central pixel with its neighbors later in
222 this section. In the noise reduction process, a 5×5 window size (i.e., 25 bins in total) is
223 specified for the low pass filter, which is empirically determined by visually comparing
224 the cloud masks with original images. We should keep in mind that the window size
225 must be limited to a medium size since a small window size is less effective in noise
226 reduction but a large window is not suitable for recognizing weak signals.

227 For performing the noise reduction with Eq. (4) in a 5×5 filter window, the number
228 of range bins (N_s) with signal greater than $S_o + 3\sigma_o$ are first counted. These N_s range
229 bins are then subtracted from the total 25 of the range bins in the filter window. Note
230 that a noise reduction is only applied when the central pixel is among the $25 - N_s$ bins,
231 and the δ function is set to be zero for the N_s range bins. If the remaining $25 - N_s$ range



232 bins are all noises, the range bin number (N_m) with SNR greater than $S_o + \sigma_o$ should
233 be about equal to an integral number (N_t) of $0.16 \times (25 - N_s)$ where 0.16 is the probability
234 for a remaining range bin to have a value greater than $S_o + \sigma_o$ for a Gaussian noise.
235 Thus when N_m is equal to or smaller than N_t , all the $25 - N_s$ range bins could only
236 contain pure noise and/or some weak cloud signals. In this case, the δ function is set
237 to 1 for all the $25 - N_s$ bins. When N_m is found to be larger than N_t , the $25 - N_s$ range
238 bins might contain a combination of moderate signal, noise and/or some weak clouds.
239 In this case, $S_o + \sigma_o$ is selected as a threshold to determine whether the neighboring
240 pixels are on the same side of the central pixel. If the central pixel has a value greater
241 than $S_o + \sigma_o$, the δ function is assigned to 1 for the $25 - N_s$ pixels with $\text{SNR} \geq S_o +$
242 σ_o , but 0 for the neighboring bins with $\text{SNR} < S_o + \sigma_o$. If the central pixel is less than
243 $S_o + \sigma_o$, the δ function is assigned to 1 for the neighboring pixels with $\text{SNR} < S_o +$
244 σ_o , but 0 for the $25 - N_s$ bins with $\text{SNR} \geq S_o + \sigma_o$.

245 After picking out the strong return signals and applying the noise reduction scheme,
246 the new background noise S_n and its standard deviation σ_n are estimated. While S_n is
247 the same as S_o , the σ_n is significantly reduced, which is a half of σ_o . This will make
248 it possible to identify more hydrometeors as exhibited in Fig.2a. We assign different
249 confidence level values to the following initial cloud mask according to the SNR. 40 is
250 first assigned to the mask of any range bins with $\text{SNR} > S_o + 3\sigma_o$ in the original input
251 data. For the rest of the range bins after applying the noise reduction, if the $\text{SNR} >$
252 $S_n + 3\sigma_n$, the mask is assigned to be 30; if $S_n + 2\sigma_n < \text{SNR} \leq S_n + 3\sigma_n$, the mask is
253 20; if $S_n + \sigma_n < \text{SNR} \leq S_n + 2\sigma_n$, the mask is 10; and the remaining range bin mask



254 is assigned to be 0.

255 To reduce both false positives (i.e. false detections) and false negatives (i.e. failed
256 detections), the next step is to estimate whether a range gate contains significant
257 hydrometeor. Following Clothiaux et al.[2000; 1995] and Marchand et al.[2008], a 5×5
258 spatial filter is used to calculate the probability of clouds and noise occurring in the 25
259 range gates. The probability of central pixel weighting scheme proposed by Marchand
260 et al. [2008] is adopted, and the weighting for the central pixel is assigned according to
261 its initial mask value. The probability is calculated by

$$262 \quad p = G(L)(0.16^{N_T})(0.84^{N_0}) \quad (5)$$

263 where N_0 is the number of masks with zeros values, N_T is the number of masks with
264 non-zeros values and $N_0 + N_T = 25$; $G(L)$ is the weighting probability of the central
265 pixel that could be a false detection where L is the significant level in the initial cloud
266 mask [$G(0)=0.84$, $G(10)=0.16$, $G(20)=0.028$, $G(\geq 30)=0.002$]. If p estimated from Eq.
267 (5) is less than a given threshold (p_{thresh}), then the central pixel is likely to be a
268 hydrometeor signal. The value in the cloud mask will set to be the same value as in the
269 initial mask if it is non-zero; otherwise it will be set to 10. Likewise, if $p > p_{thresh}$,
270 then the central pixel is likely to be noise and will be set to 0. This process is iterated 5
271 times for each pixel to obtain the final cloud mask.

272 Following Marchand et al. [2008] who well explained the logic of choosing a proper
273 threshold, p_{thresh} is calculated as

$$274 \quad p_{thresh} = (0.16^{N_{thresh}})(0.84^{25-N_{thresh}}) \quad (6)$$

275 Note that a larger p_{thresh} will keep the false positives lower but increase the false negative.



276 Herein the p_{thresh} of 5.0×10^{-12} used in Clothiaux et al.[2000], which is approximately
277 equivalent to $N_{\text{thresh}} = 13$, is selected.

278 4. Results

279 4.1 Detection test

280 To test the performance of our hydrometeor detection method, we create 7 squares
281 of SNR with sides of 100, 50, 25, 15, 10, 5, and 3 bins to mimic the radar “time-height”
282 observations as shown in Fig. 4. The background noise is randomly given by a Gaussian
283 distribution with a mean S_0 and a standard deviation σ_0 . The targets in panels a_1 , a_2
284 and a_3 are set with different SNR values to represent situations in which clouds have
285 strong, moderate and weak signals, respectively. In panel a_1 , the targets signals are set
286 to be $S_0 + 10\sigma_0$. In panel a_2 , the targets signals distribute from $S_0 + \sigma_0$ to $S_0 + 3\sigma_0$
287 with a mean value of $S_0 + 2\sigma_0$. In panel a_3 , the targets SNRs range from S_0 to $S_0 +$
288 σ_0 with a mean value of $S_0 + 0.5\sigma_0$.

289 The three middle panels in Fig. 4 show the results after applying the noise reduction.
290 Comparing with the input signals, we can see that the background noise is well
291 compressed and becomes more smooth. The shapes of the square targets are all well
292 maintained with sharp boundaries for strong and moderate signals (see panels b_1 and
293 b_2). In panel b_3 for weak signals, the 3-bin square target is not obvious while the other
294 6 squares are still distinguishable. To separate the compressed background noise from
295 hydrometeor signals, the 5×5 spatial filter is further applied to the noise-reduced data.
296 The three right panels in Fig.4 show the final mask results. Generally, the hydrometeor
297 detection method works quite good. Six of the seven square targets can be identified



298 for clouds with strong and moderate SNR. The 3×3 square is missed because the small
299 targets cannot be resolved by the 5×5 spatial filter. Since the temporal resolution of
300 KAZR is about 4 seconds, we expect that a cloud only having 3 bins in horizontal would
301 be rare in nature. For the targets with weak SNR values, the 3×3 and 5×5 square targets
302 are missed, but the rest five square targets are successfully distinguished and their
303 boundaries are well maintained.

304 To further demonstrate the performance of our method to detect the hypothetical
305 clouds in Fig.4 a1, a2, and a3, the false and failed detection rates are listed in the table
306 1. For strong signals, no background noise pixel is misidentified as one containing
307 hydrometeors at level 40. Although at levels less than 40, some noise pixels around the
308 edges of targets are identified as signals, the false detection is within 0.05%. The failed
309 detection rate is about 0.24%. For moderate signals, the failed detection rate is still as
310 small as 0.23%, while the false detection increases a little to 0.10% at the confidence
311 levels below 30. The failed detection can reach up to 9.77% for weak signal at level 10,
312 but more than 90% weak signals can be captured in our method. Note that the false
313 positive is less than 0.01%; in other words, any range gate that is detected likely as a
314 signal bin will have extremely high likelihood to contain hydrometeors.

315 The simple square clouds are also tested by using the ARM operational hydrometeor
316 detection algorithm that does not include the noise reduction and weighting schemes.
317 As can be seen in Fig. 5, the ARM operational algorithm can only find five of the seven
318 square targets with strong and moderate SNR. Meanwhile without central pixel
319 weighting, the corners of the targets become rounded and more than 2.23% of



320 hydrometeors are missed for strong and moderate cloud cases. Without the noise
321 reduction, none of the weak cloud signals can be detected. Comparing Fig.4 and Fig.5,
322 it is obvious that our hydrometeor detection method can well maintain the cloud
323 boundary, keep both false and failed detection rate as low as a few percent for strong
324 and moderate cloud cases, and has a remarkable advantage in recognizing weak signals.

325

326 4.2 Application to the SACOL KAZR observations

327 Our hydrometeor detection method was then applied to one winter and one summer
328 month (January and July in 2014) KAZR data at the SACOL. Figures 6 a, b and c show
329 an one-day example of radar reflectivity and the cloud masks from our detection method
330 and the ARM operational method without the noise reduction and the central pixel
331 weighting, respectively. A micropulse lidar (MPL) transmitted at 527 nm is operated
332 nearby the KAZR. Lidar is more sensitive to thin cirrus clouds and thus used to assess
333 the performance of our algorithm. The lidar normalized backscatter intensity and the
334 feature mask derived by modifying the method in Thorsen et al. [2015] and Thorsen
335 and Fu [2015] are shown in Fig. 6 d and e, respectively. The vertical and horizontal
336 resolutions of the radar and lidar are different, and we map the observed data and
337 derived feature mask on the same height and time coordinates for a simple comparison.
338 A distinct thin feature layer appears at about 8 km during 1500 to 1830 UTC from the
339 lidar observation which is clearly identified as a cirrus cloud using the depolarization
340 ratio. The contrast between the cirrus layer and background from the KAZR observation
341 (Fig. 6a) is very weak, and only a few range gates are identified as the ones containing



342 hydrometeors using the method without the noise reduction and weighting (Fig. 6c).
343 This thin cirrus, however, is well captured by our cloud mask method (Fig. 6b). Much
344 more cirrus range gates can be detected, although some upper portions of the full cirrus,
345 which may consist of relatively smaller ice crystals, are missed. Another apparent
346 discrepancy exists in the low atmosphere layer. A non-negligible number of range gates
347 at about 2 km are recognized as hydrometeor echoes by our method but mostly missed
348 by former technique. This feature layer is also apparent in lidar observations with
349 relative large backscatter intensities. MPL recognizes this feature as an aerosol layer.
350 In our KAZR observations, we did find some dust events that were detected by this
351 millimeter wavelength radar (see the auxiliary Fig.1). Those hydrometeor echoes
352 detected by our method might partly be caused by large dust particles.

353 The upper two panels in Fig. 7 compares the number of occurrences of the detected
354 hydrometeor range bins from our new methods with that from the ARM operational
355 algorithm for the two months of data. Generally, one can see that the variations of the
356 identified hydrometeor numbers with height from the two techniques are in a good
357 agreement. The distinct discrepancies appear at about 2 km in January and above 13
358 km in July where our method apparently identify more hydrometeors. To illustrate the
359 improvements of our method and quantitatively evaluate the two schemes used in the
360 algorithm, we plot the percent change of the detected hydrometeor bins from our
361 method comparing with that from the ARM operational method in the lower two panels
362 in Fig. 7. As expected from the results in the test square clouds, our method can identify
363 more signals. The remarkable feature is that the increased percentage is over 20% at



364 high altitude, indicating that our method can recognize more wispy-high-level cirrus
365 clouds. The increased percentage of hydrometeor derived only with the weighting
366 scheme (dashed line) and with both the noise reduction and weighting schemes (solid
367 line) are separated to demonstrates the individual contribution of the scheme to the
368 improvement of our method. In January, the number of the detected hydrometeors only
369 with the weighting scheme is almost the same as that from the ARM operational method
370 at layer from 3.5 to 9 km AGL, while this number will increase by about 5% if the noise
371 reduction scheme is involved, indicating that some hydrometeors with weak SNR
372 values may exit in this layer. Above and below this atmospheric layer, the increased
373 percentage is largely determined by the weighting scheme. In July, the two line almost
374 overlap each other between 3.5 and 9.5 km with values below 5%, revealing that the
375 bins found by our method in the middle atmospheric layer are mainly around the
376 boundaries of clouds. We may infer that in summer season, clouds in middle level are
377 usually composed of large droplets with strong SNR values. The two lines are gradually
378 apart with height. This is because hydrometeors in the upper of troposphere are usually
379 with smaller size and cause weak SNR values that will be effectively detected by the
380 noise reduction scheme.

381

382 5. Summary and Discussion

383 Based on image noise reduction technique, we propose a new method to detect
384 hydrometeors from cloud radar return signals. The basic idea is to treat the SNR value
385 of each range gate as a pixel brightness and suppress the SNR distributions of noise to



386 a narrow range by convolving with a 2-D bilateral kernel. After the noise smoothing
387 process, a special filter with central-pixel weighting scheme is used to get the final
388 cloud mask. The test square clouds show that there are two remarkable advantages of
389 our method: First the noise reduction scheme of our algorithm can enhance the contrast
390 between signal and noise, while keeping the cloud boundaries preserved and detecting
391 more hydrometeors with weak SNR values. Second both false positive and failed
392 negative rates for strong and moderate clouds can be reduced to acceptably small values.
393 A comparison of radar and lidar observed case further highlight the advantage of our
394 method in application.

395 Note that CloudSat cloud mask may have a large false detection for weak echoes. We
396 are actively working to apply our new detection method to CloudSat observations.

397

398 *Acknowledgements:* This work was supported by the National Science Foundation of
399 China (41430425, 41575016, 41521004, 41505011), China 111 project (No.B 13045),
400 and the Fundamental Research Funds for the Central University (lzujbky-2016-k01).



- 401 Reference
- 402 Ackerman, T. P., and G. M. Stokes (2003), The Atmospheric Radiation Measurement
- 403 program (vol 56, pg 38, 2003), *Physics Today*, 56(2), 14-14.
- 404 Barker, H. W. (2000), Indirect aerosol forcing by homogeneous and inhomogeneous
- 405 clouds, *Journal of Climate*, 13(22), 4042-4049, doi:10.1175/1520-
- 406 0442(2000)013<4042:iafbha>2.0.co;2.
- 407 Barker, H. W., and Q. Fu (2000), Assessment and optimization of the gamma-weighted
- 408 two-stream approximation, *Journal of the Atmospheric Sciences*, 57(8), 1181-1188,
- 409 doi:10.1175/1520-0469(2000)057<1181:aaootg>2.0.co;2.
- 410 Bony, S., et al. (2015), Clouds, circulation and climate sensitivity, *Nature Geoscience*,
- 411 8(4), 261-268, doi:10.1038/ngeo2398.
- 412 Canny, J. (1986), A COMPUTATIONAL APPROACH TO EDGE-DETECTION, *Ieee*
- 413 *Transactions on Pattern Analysis and Machine Intelligence*, 8(6), 679-698.
- 414 Clothiaux, E. E., T. P. Ackerman, G. G. Mace, K. P. Moran, R. T. Marchand, M. A.
- 415 Miller, and B. E. Martner (2000), Objective determination of cloud heights and radar
- 416 reflectivities using a combination of active remote sensors at the ARM CART sites,
- 417 *Journal of Applied Meteorology*, 39(5), 645-665, doi:10.1175/1520-
- 418 0450(2000)039<0645:odocha>2.0.co;2.
- 419 Clothiaux, E. E., M. A. Miller, B. A. Albrecht, T. P. Ackerman, J. Verlinde, D. M. Babb,
- 420 R. M. Peters, and W. J. Syrett (1995), AN EVALUATION OF A 94-GHZ RADAR FOR
- 421 REMOTE-SENSING OF CLOUD PROPERTIES, *Journal of Atmospheric and*
- 422 *Oceanic Technology*, 12(2), 201-229, doi:10.1175/1520-



- 423 0426(1995)012<0201:aeoagr>2.0.co;2.
- 424 Clothiaux, E. E., K. P. Moran, B. E. Martner, T. P. Ackerman, G. G. Mace, T. Uttal, J.
- 425 H. Mather, K. B. Widener, M. A. Miller, and D. J. Rodriguez (1999), The atmospheric
- 426 radiation measurement program cloud radars: Operational modes, *Journal of*
- 427 *Atmospheric and Oceanic Technology*, 16(7), 819-827, doi:10.1175/1520-
- 428 0426(1999)016<0819:tarmpc>2.0.co;2.
- 429 Fu, Q. (2007), A new parameterization of an asymmetry factor of cirrus clouds for
- 430 climate models, *Journal of the Atmospheric Sciences*, 64(11), 4140-4150,
- 431 doi:10.1175/2007jas2289.1.
- 432 Fu, Q., M. Baker, and D. L. Hartmann (2002), Tropical cirrus and water vapor: an
- 433 effective Earth infrared iris feedback?, *Atmospheric Chemistry and Physics*, 2, 31-37.
- 434 Fu, Q., B. Carlin, and G. Mace (2000a), Cirrus horizontal inhomogeneity and OLR bias,
- 435 *Geophysical Research Letters*, 27(20), 3341-3344, doi:10.1029/2000gl011944.
- 436 Fu, Q., M. C. Cribb, and H. W. Barker (2000b), Cloud geometry effects on atmospheric
- 437 solar absorption, *Journal of the Atmospheric Sciences*, 57(8), 1156-1168.
- 438 He, K., J. Sun, and X. Tang (2013), Guided Image Filtering, *Ieee Transactions on*
- 439 *Pattern Analysis and Machine Intelligence*, 35(6), 1397-1409,
- 440 doi:10.1109/tpami.2012.213.
- 441 Huang, J. P. (2006), Analysis of ice water path retrieval errors over tropical ocean,
- 442 *Advances in Atmospheric Sciences*, 23(2), 165-180, doi:10.1007/s00376-006-0165-4.
- 443 Huang, J. P., P. Minnis, B. Lin, Y. H. Yi, T. F. Fan, S. Sun-Mack, and J. K. Ayers (2006a),
- 444 Determination of ice water path in ice-over-water cloud systems using combined



- 445 MODIS and AMSR-E measurements, *Geophysical Research Letters*, 33(21),
446 doi:10.1029/2006gl027038.
- 447 Huang, J. P., P. Minnis, B. Lin, Y. H. Yi, M. M. Khaiyer, R. F. Arduini, A. Fan, and G.
448 G. Mace (2005), Advanced retrievals of multilayered cloud properties using
449 multispectral measurements, *Journal of Geophysical Research-Atmospheres*, 110(D15),
450 doi:10.1029/2004jd005101.
- 451 Huang, J. P., Y. J. Wang, T. H. Wang, and Y. H. Yi (2006b), Dusty cloud radiative forcing
452 derived from satellite data for middle latitude regions of East Asia, *Progress in Natural
453 Science*, 16(10), 1084-1089.
- 454 Huang, J. P., et al. (2008), An Overview of the Semi-arid Climate and Environment
455 Research Observatory over the Loess Plateau, *Advances in Atmospheric Sciences*, 25(6),
456 906-921, doi:10.1007/s00376-008-0906-7.
- 457 Illingworth, A. J., et al. (2007), Cloudnet - Continuous evaluation of cloud profiles in
458 seven operational models using ground-based observations, *Bulletin of the American
459 Meteorological Society*, 88(6), 883+, doi:10.1175/bams-88-6-883.
- 460 King, M. D., S. Platnick, W. P. Menzel, S. A. Ackerman, and P. A. Hubanks (2013),
461 Spatial and Temporal Distribution of Clouds Observed by MODIS Onboard the Terra
462 and Aqua Satellites, *Ieee Transactions on Geoscience and Remote Sensing*, 51(7), 3826-
463 3852, doi:10.1109/tgrs.2012.2227333.
- 464 Kollias, E. E. Clothiaux, M. A. Miller, B. A. Albrecht, G. L. Stephens, and T. P.
465 Ackerman (2007a), Millimeter-wavelength radars - New frontier in atmospheric cloud
466 and precipitation research, *Bulletin of the American Meteorological Society*, 88(10),



467 1608-+, doi:10.1175/bams-88-10-1608.

468 Kollias, E. E. Clothiaux, M. A. Miller, E. P. Luke, K. L. Johnson, K. P. Moran, K. B.
469 Widener, and B. A. Albrecht (2007b), The Atmospheric Radiation Measurement
470 Program cloud profiling radars: Second-generation sampling strategies, processing, and
471 cloud data products, *Journal of Atmospheric and Oceanic Technology*, 24(7), 1199-
472 1214, doi:10.1175/jtech2033.1.

473 Li, J., J. Huang, K. Stamnes, T. Wang, Q. Lv, and H. Jin (2015), A global survey of
474 cloud overlap based on CALIPSO and CloudSat measurements, *Atmospheric
475 Chemistry and Physics*, 15(1), 519-536, doi:10.5194/acp-15-519-2015.

476 Mace, G. G., T. P. Ackerman, P. Minnis, and D. F. Young (1998), Cirrus layer
477 microphysical properties derived from surface-based millimeter radar and infrared
478 interferometer data, *Journal of Geophysical Research-Atmospheres*, 103(D18), 23207-
479 23216, doi:10.1029/98jd02117.

480 Mace, G. G., E. E. Clothiaux, and T. P. Ackerman (2001), The composite characteristics
481 of cirrus clouds: Bulk properties revealed by one year of continuous cloud radar data,
482 *Journal of Climate*, 14(10), 2185-2203, doi:10.1175/1520-
483 0442(2001)014<2185:tccocc>2.0.co;2.

484 Marchand, R., G. G. Mace, T. Ackerman, and G. Stephens (2008), Hydrometeor
485 detection using Cloudsat - An earth-orbiting 94-GHz cloud radar, *Journal of
486 Atmospheric and Oceanic Technology*, 25(4), 519-533, doi:10.1175/2007jtecha1006.1.

487 Marr, D., and E. Hildreth (1980), THEORY OF EDGE-DETECTION, *Proceedings of
488 the Royal Society Series B-Biological Sciences*, 207(1167), 187-217,



489 doi:10.1098/rspb.1980.0020.

490 Perona, P., and J. Malik (1990), SCALE-SPACE AND EDGE-DETECTION USING

491 ANISOTROPIC DIFFUSION, *Ieee Transactions on Pattern Analysis and Machine*

492 *Intelligence*, 12(7), 629-639, doi:10.1109/34.56205.

493 Protat, A., D. Bouniol, J. Delanoe, P. T. May, A. Plana-Fattori, A. Hasson, E. O'Connor,

494 U. Goersdorf, and A. J. Heymsfield (2009), Assessment of Cloudsat Reflectivity

495 Measurements and Ice Cloud Properties Using Ground-Based and Airborne Cloud

496 Radar Observations, *Journal of Atmospheric and Oceanic Technology*, 26(9), 1717-

497 1741, doi:10.1175/2009jtecha1246.1.

498 Protat, A., J. Delanoe, P. T. May, J. Haynes, C. Jakob, E. O'Connor, M. Pope, and M. C.

499 Wheeler (2011), The variability of tropical ice cloud properties as a function of the

500 large-scale context from ground-based radar-lidar observations over Darwin, Australia,

501 *Atmospheric Chemistry and Physics*, 11(16), 8363-8384, doi:10.5194/acp-11-8363-

502 2011.

503 Ramanathan, V., R. D. Cess, E. F. Harrison, P. Minnis, B. R. Barkstrom, E. Ahmad, and

504 D. Hartmann (1989), CLOUD-RADIATIVE FORCING AND CLIMATE - RESULTS

505 FROM THE EARTH RADIATION BUDGET EXPERIMENT, *Science*, 243(4887), 57-

506 63, doi:10.1126/science.243.4887.57.

507 Randall, D. A., R.A. Wood, S. Bony, R. Colman, T. Fichefet, J. Fyfe, V. Kattsov, A.

508 Pitman, J. Shukla, J. Srinivasan, R.J. Stouffer, A. Sumi and K.E. Taylor (2007), Climate

509 Models and Their Evaluation. In: *Climate Change 2007: The Physical Science Basis,*

510 *Contribution of Working Group I to the Fourth Assessment Report of the*



- 511 *Intergovernmental Panel on Climate Change, [Solomon, S., D. Qin, M. Manning, Z.*
512 *Chen, M. Marquis, K.B. Averyt, M. Tignor and H.L. Miller (eds.)]. Cambridge*
513 *University Press, Cambridge, United Kingdom and New York, NY, USA.*
- 514 Sassen, K., and S. Benson (2001), A midlatitude cirrus cloud climatology from the
515 facility for atmospheric remote sensing. Part II: Microphysical properties derived from
516 lidar depolarization, *Journal of the Atmospheric Sciences*, 58(15), 2103-2112,
517 doi:10.1175/1520-0469(2001)058<2103:amcccf>2.0.co;2.
- 518 Stephens, G. L. (2005), Cloud feedbacks in the climate system: A critical review,
519 *Journal of Climate*, 18(2), 237-273, doi:10.1175/jcli-3243.1.
- 520 Stephens, G. L., et al. (2002), The cloudsat mission and the a-train - A new dimension
521 of space-based observations of clouds and precipitation, *Bulletin of the American*
522 *Meteorological Society*, 83(12), 1771-1790, doi:10.1175/bams-83-12-1771.
- 523 Su, J., J. Huang, Q. Fu, P. Minnis, J. Ge, and J. Bi (2008), Estimation of Asian dust
524 aerosol effect on cloud radiation forcing using Fu-Liou radiative model and CERES
525 measurements, *Atmospheric Chemistry and Physics*, 8(10), 2763-2771.
- 526 Thorsen, and Q. Fu (2015), Automated Retrieval of Cloud and Aerosol Properties from
527 the ARM Raman Lidar. Part II: Extinction, *Journal of Atmospheric and Oceanic*
528 *Technology*, 32(11), 1999-2023, doi:10.1175/jtech-d-14-00178.1.
- 529 Thorsen, Q. Fu, and J. Comstock (2011), Comparison of the CALIPSO satellite and
530 ground-based observations of cirrus clouds at the ARM TWP sites, *Journal of*
531 *Geophysical Research-Atmospheres*, 116, doi:10.1029/2011jd015970.
- 532 Thorsen; Fu, Q. N., Rob K.; Turner David D.; Comstock Jennifer M. (2015), Automated

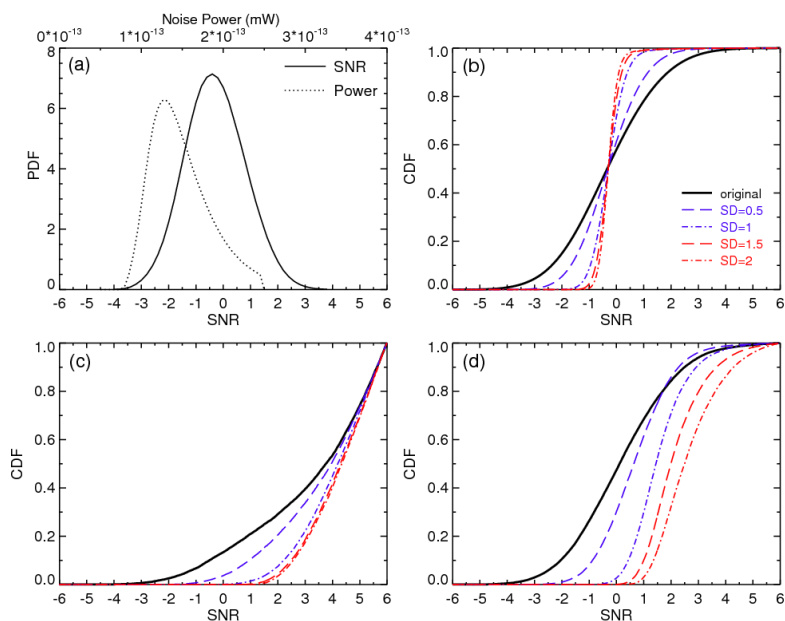


- 533 Retrieval of Cloud and Aerosol Properties from the ARM Raman Lidar. Part I: Feature
534 Detection, *JOURNAL OF ATMOSPHERIC AND OCEANIC TECHNOLOGY*, 32(11),
535 1977-1998, doi:10.1175/JTECH-D-14-00150.1.
- 536 Tomasi, C., and R. Manduchi (1998), Bilateral Filtering for Gray and Color Images,
537 *IEEE International Conference on Computer Vision, Bombay, India*,
538 doi:10.1109/ICCV.1998.710815.
- 539 Wang, Z., and K. Sassen (2001), Cloud type and macrophysical property retrieval using
540 multiple remote sensors, *Journal of Applied Meteorology*, 40(10), 1665-1682,
541 doi:10.1175/1520-0450(2001)040<1665:ctampr>2.0.co;2.
- 542 Williams, K. D., and M. J. Webb (2009), A quantitative performance assessment of
543 cloud regimes in climate models, *Climate Dynamics*, 33(1), 141-157,
544 doi:10.1007/s00382-008-0443-1.
- 545 Yan, H. R., J. P. Huang, P. Minnis, Y. H. Yi, S. Sun-Mack, T. H. Wang, and T. Y.
546 Nakajima (2015), Comparison of CERES-MODIS cloud microphysical properties with
547 surface observations over Loess Plateau, *Journal of Quantitative Spectroscopy &*
548 *Radiative Transfer*, 153, 65-76, doi:10.1016/j.jqsrt.2014.09.009.
- 549 Yuan, J., Q. Fu, and N. McFarlane (2006), Tests and improvements of GCM cloud
550 parameterizations using the CCCMA SCM with the SHEBA data set, *Atmospheric*
551 *Research*, 82(1-2), 222-238, doi:10.1016/j.atmosres.2005.10.009.

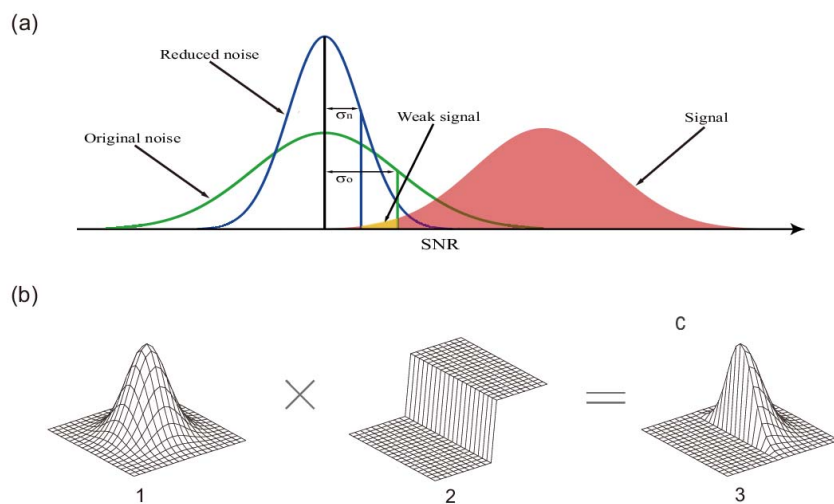


Cloud Type	Performance (%)	Cloud Mask Confidence Level			
		≥10	≥20	≥30	≥40
Strong	False positive	0.048	0.044	0.009	0
	Failed negative	0.244	0.244	0.244	0.244
Moderate	False positive	0.103	0.103	0.063	0
	Failed negative	0.229	0.229	0.229	100
Weak	False positive	0.007	0.006	0.003	0
	Failed negative	9.774	96.788	100	100

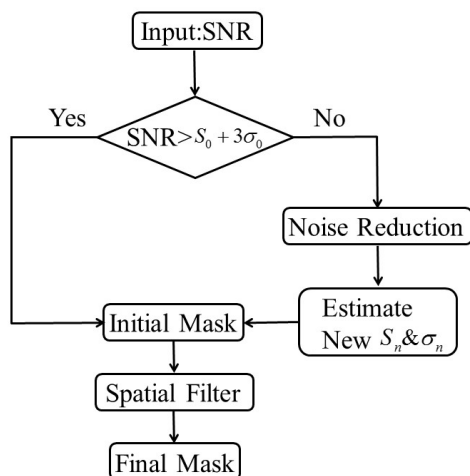
552 Table 1. Summary of false positives and failed negatives for hypothetical strong,
553 moderate and weak cloud cases in Fig.4 a1, a2, and a3, respectively.



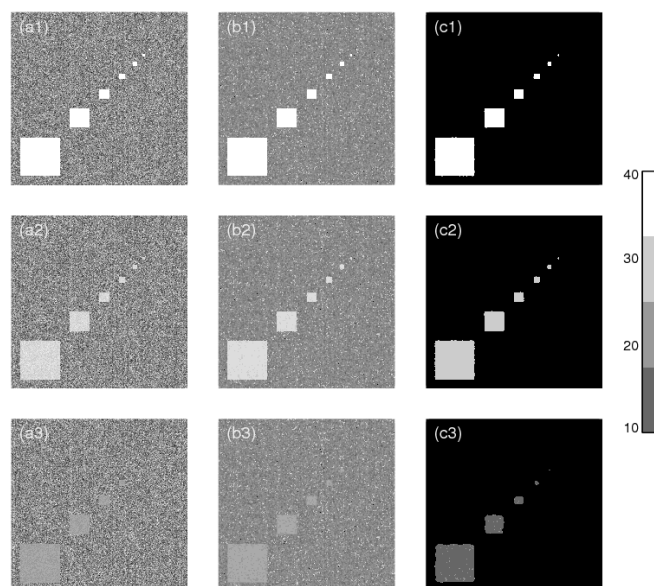
554 Figure 1. (a) Probability distribution function (PDF) of the noise power and SNR from
555 the KAZR observations in a clear day of January 21, 2014. (b) Cumulative distribution
556 function (CDF) of original and convolved SNR for the noise from the clear day. (c) and
557 (d) CDF of original and convolved SNR from a cloudy case of January 4, 2014 for
558 range gates inside and outside the cloud adjacent to the cloud boundary, respectively.



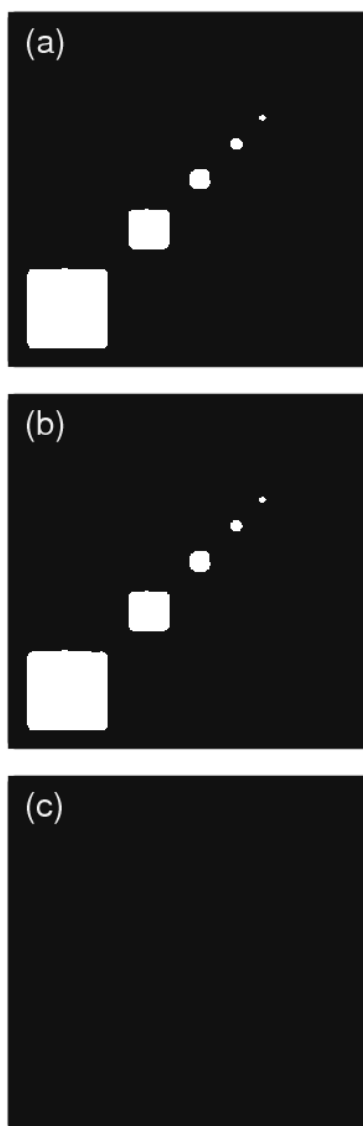
559 Figure 2. (a) comparison of original noise, reduced noise and hydrometeor signal
560 distributions. (b) Illustration of the bilateral filtering process. (b1) Gaussian kernel
561 distribution in space. (b2) δ function. (b3) Bilateral kernel by combining Gaussian
562 kernel with δ function.
563



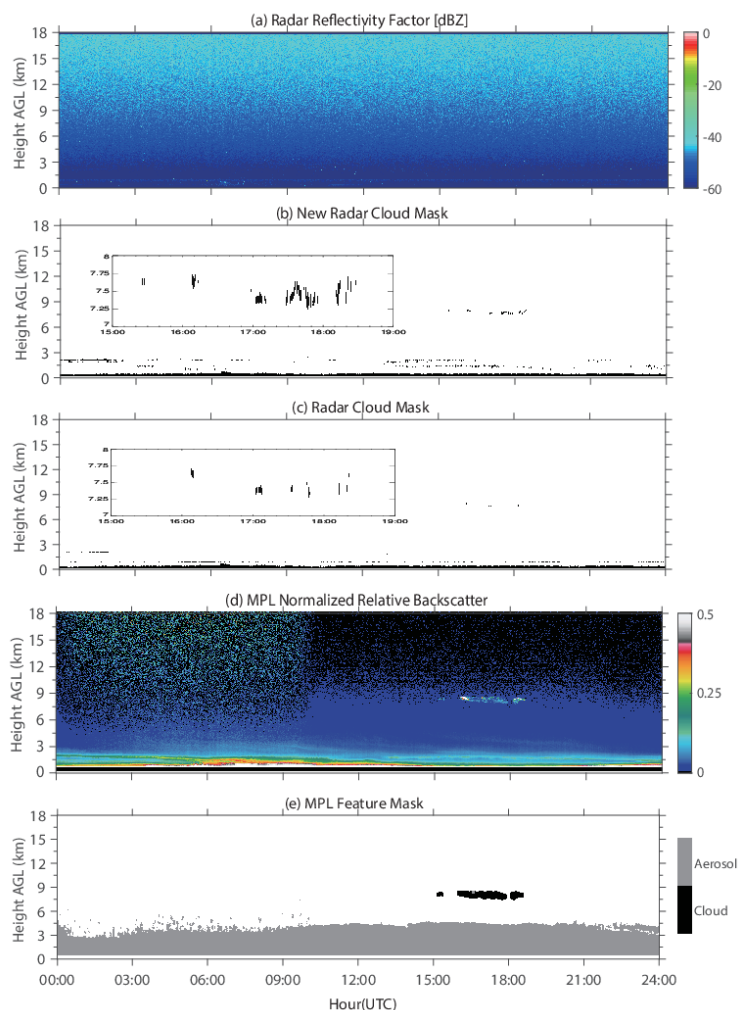
564 Figure 3. Schematic flow diagram for hydrometeor detection method.



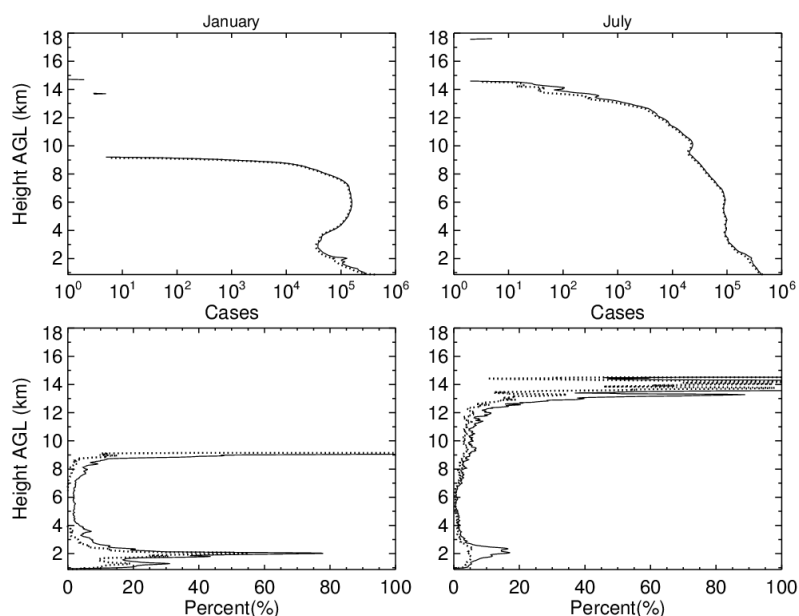
565 Figure 4. Panels a₁, a₂ and a₃ are three “square clouds” that have strong, moderate and
566 weak SNR values with random Gaussian noise used to test the detection method. Panels
567 b₁, b₂ and b₃ are SNR distributions after convolving the data with a bilateral kernel.
568 Panels c₁, c₂ and c₃ are the final cloud mask filtered by the spatial filter.



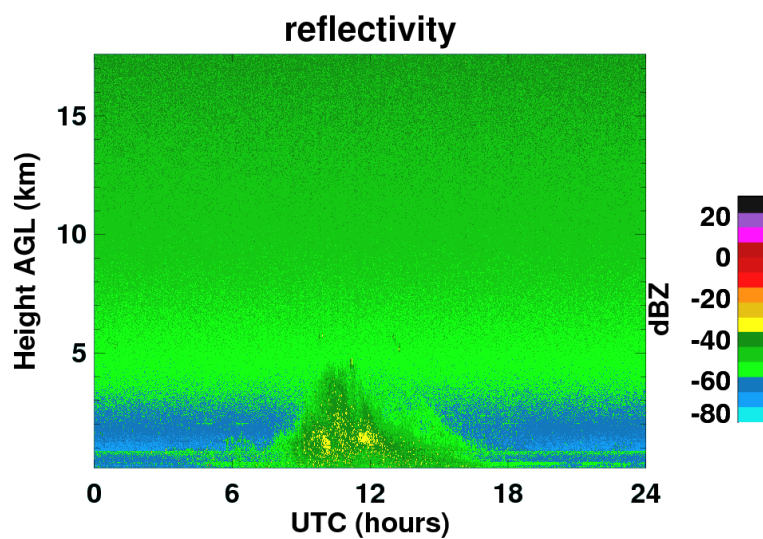
569 Figure 5. Cloud mask without applying noise reduction and central pixel weighting. (a),
570 (b), (c) are for the targets with strong, moderate and weak SNR, respectively, from Fig.
571 4 a1, a2, and a3.



572 Figure 6. One-day example of radar- and lidar-observed cirrus cloud at the SACOL on
573 January 8, 2014. (a) KAZR reflectivity. (b) radar cloud mask derived by our new
574 method. (c) radar cloud mask derived by the ARM operational algorithm. (d) MPL
575 normalized backscatter intensity. (e) MPL feature mask. Two windows in (b), (c) show
576 the zoom-in views of cirrus masks.



577 Figure 7. The upper panel shows the number of occurrences of the detected
578 hydrometeor range bins from the two methods. The solid line represents the results
579 derived from our new method. The dashed line is from the ARM operational method.
580 The lower two panels demonstrate the increased percentage of hydrometeor bins from
581 our new method comparing to the ARM operational method. The solid line is calculated
582 by applying both noise reduction and central-pixel weighting schemes, while the dashed
583 line is calculated by only applying the central-pixel weighting scheme in our detection
584 method.



585 Auxiliary Figure 1. A dust event observed on January 29th, 2014. The morphology and
586 power level of the return signal is apparent not for a cloud from the surface to the height
587 of 5 km between 0800 to 1600 UTC.